Journal of Power Sources 323 (2016) 201–212

Contents lists available at ScienceDirect

Journal of Power Sources

journal homepage: www.elsevier.com/locate/jpowsour

Numerical study of droplet dynamics in a polymer electrolyte fuel cell gas channel using an embedded Eulerian-Lagrangian approach

Alex Jarauta [a, *], Pavel Ryzhakov [a], Marc Secanell [b], Prashant R. Waghmare [c], Jordi Pons-Prats [a]

[a] Centre Internacional de Mètodes Numèrics en Enginyeria (CIMNE), Gran Capitán s/n, 08034 Barcelona, Spain
[b] Energy Systems Design Laboratory (ESDLab), University of Alberta, Edmonton, Canada
[c] Interfacial Science and Surface Engineering Lab (iSSELab), Department of Mechanical Engineering, University of Alberta, Edmonton, Canada

HIGHLIGHTS

- We model the droplet dynamics on a PEFC cathode gas channel with a novel technique.
- A simple method to obtain interface curvature in two dimensions is given.
- Dynamic contact angle condition for droplets on rough surfaces is presented.
- Results can predict several variables of interest and agree with experimental data.

ARTICLE INFO

Article history:
Received 19 October 2015
Received in revised form
22 April 2016
Accepted 8 May 2016
Available online 20 May 2016

Keywords:
Fuel cells
Droplet dynamics
Surface tension
Embedded

ABSTRACT

An embedded Eulerian-Lagrangian formulation for the simulation of droplet dynamics within a polymer electrolyte fuel cell (PEFC) channel is presented. Air is modeled using an Eulerian formulation, whereas water is described with a Lagrangian framework. Using this framework, the gas-liquid interface can be accurately identified. The surface tension force is computed using the curvature defined by the boundary of the Lagrangian mesh. The method naturally accounts for material property changes across the interface and accurately represents the pressure discontinuity. A sessile drop in a horizontal surface, a sessile drop in an inclined plane and droplets in a PEFC channel are solved for as numerical examples and compared to experimental data. Numerical results are in excellent agreement with experimental data. Numerical results are also compared to results obtained with the semi-analytical model previously developed by the authors in order to discuss the limitations of the semi-analytical approach.

1. Introduction

Water management is a key limiting factor of PEFCs performance [1]. Water is produced by the oxygen reduction reaction (ORR) in the cathode catalyst layer (CL) of the fuel cell. At high current densities excess liquid water is evacuated through the pores of the gas diffusion layer (GDL). When it emerges from the pores into the gas channels it may form droplets, films or slug flows depending on the working conditions [2]. Interface conditions between the channel and the GDL remain largely unknown and continue to be a very active area of research [3]. The present study proposes a novel technique to improve the numerical analysis of droplet dynamics on the GDL surface.

There are several studies in the literature that investigate droplet dynamics using an analytical approach [4–6]. The authors recently proposed a semi-analytical model that improved previous treatments of drag and adhesion forces [7]. Although these models provide solutions with low computational cost, they oversimplify the phenomena by either using predefined droplet geometries or neglecting water-air interactions. For gravity-dominated flows, such as film or slug flows, analytical models cannot describe the geometry and therefore they cannot be used [7]. Surface tension and adhesion forces strongly depend on geometry. Contact angle hysteresis, i.e, the difference between advancing and receding angles, is used to predict droplet detachment [1,8]. An accurate description of the geometry is key to model droplet dynamics.

Numerical methods can be used to provide more accurate

* Corresponding author.
E-mail address: ajarauta@cimne.upc.edu (A. Jarauta).

http://dx.doi.org/10.1016/j.jpowsour.2016.05.030
0378-7753/

droplet dynamics predictions. Several studies in the literature study the phenomena using an Eulerian formulation together with the Volume of Fluid (VOF) method [9]. A review of two and three-dimensional droplet dynamics models based on the VOF method can be found in Ref. [10].

Previous numerical simulations based on the Volume of Fluid method implement the surface tension force using the Continuum Surface Force (CSF) as a volumetric force in the momentum equation [10–11]. The formulations rely upon an explicit treatment of the surface tension. This restricts the model to using extremely small time steps (governed by the time scale associated with the propagation of capillary waves) in order to achieve convergence [12]. This restriction is an important drawback for practical PEFC simulations. Additionally, VOF studies need very fine meshes to have an accurate description of the interface. This further increases the computational cost of the corresponding simulations.

An alternative to Eulerian models are the Lagrangian models, such as the one proposed by Saksono and Perić [13]. Saksono and Perić [13] proposed a variational formulation for the surface tension term. One of the advantages of Lagrangian models is that they can track exactly the water domain and its boundary. This formulation could be used to describe quasistatic and dynamic problems [14]. The application of the model presented in Ref. [13] is however restricted to the water domain. Air-water interactions were not studied. A multi-fluid model using a pure Lagrangian formulation was presented in Ref. [15]. Results showed that steady-state solution presented spurious velocities at the interface. Lagrangian models have the additional disadvantage that the domain has to be remeshed after each time step in order to avoid mesh degradation. In the context of PEFC gas channels, a model treating both the gas and the liquid droplets in a Lagrangian framework would have a large computational cost due to remeshing.

Recently, embedded Eulerian-Lagrangian formulations have been proposed [16–17]. This approach has been shown to be advantageous for fluid-fluid problems as it restricts the mesh moving and remeshing to the liquid domain, while maintaining a fixed mesh for the gas. This approach is very well suited to study liquid drops in fuel cell channels since it allows for:

a) natural tracking of the liquid-gas interface
b) efficient partitioned implementation
c) possibility of using large time steps
d) good mass conservation

This article discusses the mathematical model, implementation and numerical validation of a novel two-dimensional Eulerian-Lagrangian embedded formulation applied to PEFC gas channel simulations. Special emphasis is given to the surface tension and contact angle conditions. For the numerical examples solved, the present formulation led to stable and accurate solutions with time steps up to 3 orders of magnitude higher than those obtained with VOF [18]. The model is implemented in two dimensions. A three-dimensional implementation of the model is underway.

The paper is organized as follows. First, the mathematical model is presented, with special attention given to the surface tension term. Next, the contact angle condition is explained, including a dynamic contact angle condition to improve numerical results of droplet deformation on rough surfaces such as GDLs. The model is then compared to sessile and inclined plane experimental results in order to validate the surface tension implementation. Droplet dynamics in a PEFC channel are studied next. A comparison of results with those found using the semi-analytical model presented by the authors in Ref. [7] is also provided. Emphasis is placed on the model capabilities since three-dimensional simulations are required to provide physically accurate results.

2. Numerical model

According to the embedded[1] approach proposed in Refs. [16,17], the two-phase problem is treated in a partitioned manner using the Eulerian and Lagrangian frameworks for air and water, respectively. In this numerical formulation, the Lagrangian sub-domain (water) is moving on top of the fixed Eulerian mesh and the interaction is represented by the boundary condition exchange across the interface. A schematic representation of the embedded air-water setting is shown in Fig. 1. The Lagrangian domain Ω_W is embedded into the Eulerian domain Ω_A. The outer boundary of the Eulerian domain is designated as Γ_A. The boundary of the Lagrangian domain Γ_I defines the position of the interface between both fluids. The intersection between both boundaries is denoted by $\Gamma_S=\Gamma_A\cap\Gamma_I$.

In the following section, the governing equations for both the subdomains and the coupling equations are specified. For further details on the embedded approach for multi-fluids the reader is referred to [17].

2.1. Governing equations

The system considered in the present work is a domain (Ω_A) filled with air and a small fraction of water (Ω_W) within it. In this case, air and water are considered incompressible Newtonian viscous fluids. The governing equations for both fluids are the Navier-Stokes equations (note that it is assumed that gas and liquid are not produced/consumed in the computational domain):

$$\nabla\cdot\mathbf{v} = 0 \text{ on } \Omega_A \text{ and } \Omega_W \tag{1}$$

$$\rho_f\frac{D\mathbf{v}}{Dt} - \nabla\cdot\boldsymbol{\sigma} = \rho_f\mathbf{g} \text{ on } \Omega_A \text{ and } \Omega_W \tag{2}$$

where $\mathbf{v}$ is the velocity vector, $\boldsymbol{\sigma}$ is the Cauchy stress tensor, t is the time, $\mathbf{g}$ is the body force and ρ_f is the fluid density. Since air is modeled using a viscous incompressible fluid formulation and thermal effects are neglected, no equation of state (such as e.g. ideal gas equation) is necessary to close the governing system. For sake of brevity, a single set of equations has been written to represent the governing equations for both fluids. The operator $\frac{D\phi}{Dt}$ stands for the total material derivative:

$$\frac{D\phi}{Dt} = \frac{\partial\phi}{\partial t} + \mathbf{v}\cdot\nabla\phi \tag{3}$$

The convective term $\mathbf{v}\cdot\nabla\phi$ is absent in the Lagrangian formulation.

2.2. Boundary conditions

Boundary conditions for both air and water domain and its interface are imposed in order to solve the problem. A no-slip Dirichlet boundary condition is imposed at Γ_A:

$$\mathbf{v}_A = 0 \text{ at } \Gamma_A \tag{4}$$

Water can have non-zero velocities on the x direction and therefore a slip boundary condition is imposed at Γ_S:

$$\mathbf{v}_W\cdot\mathbf{n} = 0 \text{ at } \Gamma_S \tag{5}$$

At the air-water interface Γ_I, two boundary conditions are

[1] In the CFD community, “embedded” refers to the setting, where a moving mesh is immersed or embedded into a fixed mesh. Alternatively, the term “immersed boundary” method is sometimes used.

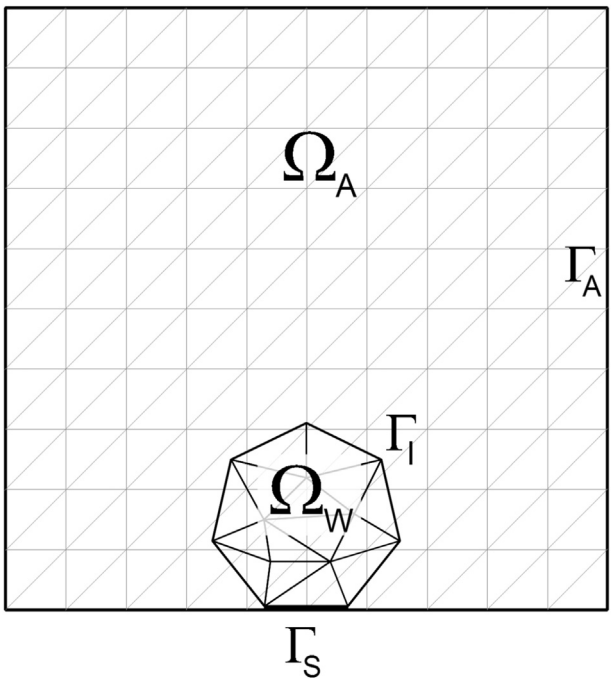

Fig. 1. Schematic representation of the embedded two-fluid system.

prescribed:

$$\mathbf{v}_W - \mathbf{v}_A = 0 \text{ at } \Gamma_I \tag{6}$$

$$[\![\boldsymbol{\sigma}]\!]\cdot\mathbf{n} = \gamma\kappa\mathbf{n} \text{ at } \Gamma_I \tag{7}$$

where $\mathbf{n}$ is the unit normal to interface Γ_I, γ is the surface tension coefficient and κ is the interface curvature. The $[\![\sigma]\!]$ symbol represents the jump in the stress across the interface.

Eq. (6) expresses the continuity of all velocity components. Equality of normal components ensures no mass flow across the interface, whereas tangential components' equality is similar to a no-slip boundary condition. Eq. (7) reads that the difference in normal stress across the interface is balanced by surface tension force. For an incompressible Newtonian fluid, the Cauchy stress tensor is given by:

$$\boldsymbol{\sigma} = -p\mathbf{I} + \mu_f\left(\nabla\mathbf{v} + \nabla^T\mathbf{v}\right) \tag{8}$$

In our work, viscous stresses on the normal direction are neglected. Projecting Eq. (7) onto normal and tangential directions and using Eq. (8) yields:

$$p_W - p_A = -\gamma\kappa \text{ at } \Gamma_I \tag{9}$$

$$\mu_A\mathbf{t}\cdot\left[\nabla\mathbf{v} + \nabla^T\mathbf{v}\right]_A\cdot\mathbf{n} - \mu_W\mathbf{t}\cdot\left[\nabla\mathbf{v} + \nabla^T\mathbf{v}\right]_W\cdot\mathbf{n} = 0 \text{ at } \Gamma_I \tag{10}$$

More details on the boundary conditions can be found in Ref. [17]. The negative sign in Eq. (9) denotes that the surface tension force is a vector pointing towards the droplet. This is usually true, unless the interface is concave.

2.2.1. Surface tension

The right-hand side term in Eq. (7) is the surface tension term, corresponding to the normal component of the stresses at the interface. This additional term can be interpreted as a Neumann boundary condition at the water surface:

$$f_{st} = -\gamma\kappa \tag{11}$$

The curvature in two dimensions is defined as follows [19,8]:

$$\kappa = \nabla_s\cdot\mathbf{n} = \left|\left|\frac{d\mathbf{n}}{ds}\right|\right| \tag{12}$$

where ∇_s is the surface gradient operator (i.e., the conventional gradient without the component normal to the surface) and $\frac{d\phi}{ds}$ is the rate of change of variable ϕ along a given curve. Eq. (12) can be interpreted as the change in direction of the normal vector along the interface. The discrete version of this equation can be implemented using subsets of three nodes at the interface. At every node I, the curvature is computed using its nearest neighbors at the interface. Let us denote the vector pointing from node $I-1$ to node I as $\mathbf{r_1}$, and the vector pointing from node I to node $I+1$ as $\mathbf{r_2}$ (Fig. 2(c)).

To find the change in direction of the contact line at node I, one must normalize the vector $\mathbf{r_1} - \mathbf{r_2}$. The normalized vectors $\mathbf{r_1}$ and $\mathbf{r_2}$ will be denoted as $\widehat{\mathbf{r}}_\mathbf{1}$ and $\widehat{\mathbf{r}}_\mathbf{2}$:

$$\widehat{\mathbf{r}}_\mathbf{k} = \frac{\mathbf{r_k}}{||\mathbf{r_k}||} \tag{13}$$

The curvature is the norm of the vector divided by the length of the polyline pointing from node $I-1$ to $I+1$:

$$\kappa = \frac{\left|\left|\widehat{\mathbf{r}}_\mathbf{1} - \widehat{\mathbf{r}}_\mathbf{2}\right|\right|}{||\mathbf{r_1}|| + ||\mathbf{r_2}||} \tag{14}$$

Eq. (14) is a direct measure of the change in direction of the tangent vector along the interface. Since tangent and normal vectors at the surface are orthogonal, the curvature value remains unaltered. In addition to the curvature, one must compute its sign at node I: if the midpoint of the line connecting the neighbors of node I is inside the water domain, then the sign is positive (convex interface). On the contrary, if the midpoint lies outside the water domain, the sign is negative and the surface tension force at node I points outwards the interface.

2.2.2. Dynamic contact angle condition

The contact angle observed is the macroscopic manifestation of equilibrium between the different surface free energies [20–21]: γ_{SL} (solid-liquid), γ_{LG} (liquid-gas) and γ_{SG} (solid-gas). From a numerical point of view, the surface tension term discussed in Sec. 2.2.1 is applied at the interface Γ_I. However, this term is slightly modified for the nodes at the contact line. At Γ_S, since curvature is zero surface tension is also zero. At the contact line Eq. (11) is solved using the normal vector corresponding to the static equilibrium configuration $\mathbf{n}_{eq}$ instead of the actual normal vector $\mathbf{n}$. Fig. 2 shows the difference between both normal vectors. The normal vector at equilibrium is constant and forms an angle θ_S with the vertical axis (Fig. 2(b)), whereas the normal vector depends on the configuration of the droplet and forms an angle θ (Fig. 2(a)). An alternative to the above approach can be found in Refs. [13,22].

When a droplet lays on a rough surface, such as those used in PEFC gas channels, the concept of *static contact angle* cannot be used. In rough surfaces, the contact line pins and the contact angle changes from one equilibrium configuration to another. The present work uses two threshold values, $\theta_{\min}$ and $\theta_{\max}$, as contact angle conditions. The contact line is fixed only within the range $\theta \in [\theta_{\min},\theta_{\max}]$. These maximum and minimum values represent the measured contact angles for incipient motion when the droplet is placed on a tilted plane. Further details of the method are discussed in section 3.2. Note also that the contact angle might not

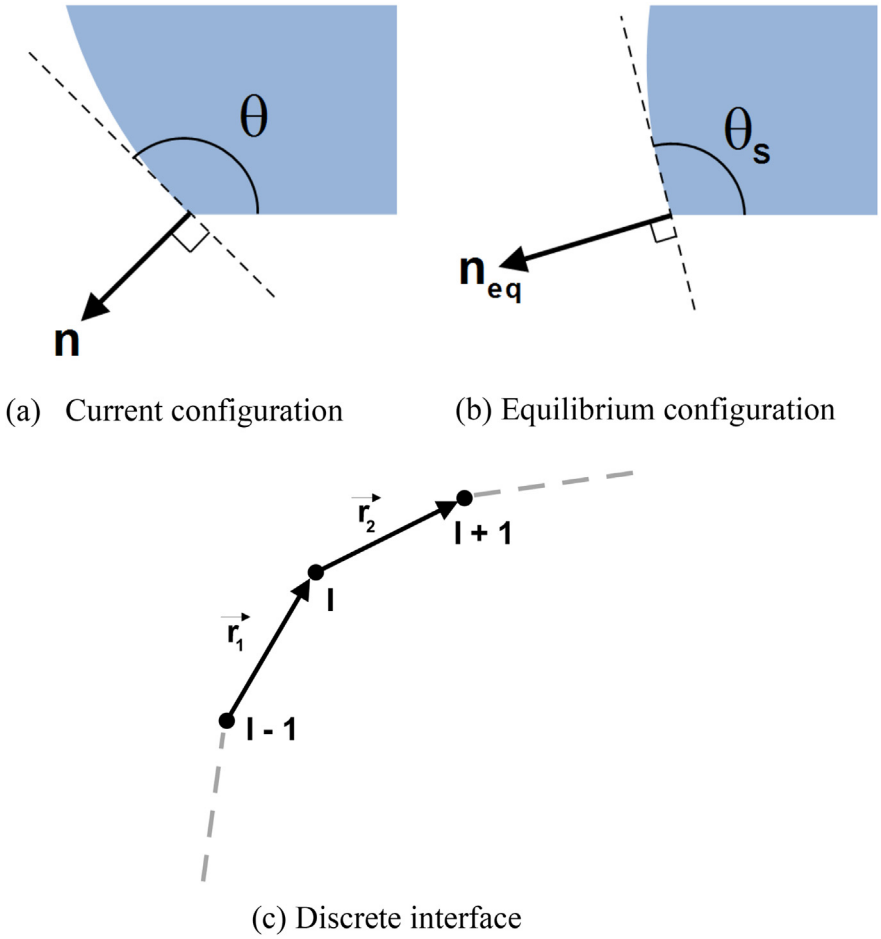

Fig. 2. (a)–(b) Normal vector and contact angle at current and equilibrium configurations and (c) Discretization of the air-water interface.

correspond to that of the material due to surface roughness as described by Wenzel and Cassie-Baxter models.

It is important to note that the presented formulation does not model the roughness of the porous substrate (GDL). The dynamic contact angle condition represents a first step towards including roughness effects in the model. Substrate roughness will be included in future publications.

2.3. Solution strategy

2.3.1. FEM discretization

We use standard mixed FEM with linear interpolations for the velocity and the pressure values over 3-noded triangles for the spatial discretization of the governing equations (Eqs. (1) and (2)). Backward Euler is used as the time integration scheme for simplicity, although any θ-method can be used for time integration.

Given $\overline{\mathbf{v}}_n$ and $\overline{p}_n$ at t_n, the time discrete problem consists in finding $\overline{\mathbf{v}}_{n+1}$ and $\overline{p}_{n+1}$ at t_{n+1} as the solution of

$$\overline{\mathbf{r}}_m = \overline{\mathbf{F}} - \mathbf{M}\frac{\overline{\mathbf{v}}_{n+1} - \overline{\mathbf{v}}_n}{\Delta t} - \left[\overline{\mathbf{K}}(\overline{\mathbf{v}}_{n+1}) + \mu\mathbf{L}\right]\overline{\mathbf{v}}_{n+1} - \mathbf{G}\overline{p}_{n+1} = 0 \tag{15}$$

$$\overline{\mathbf{r}}_c = \mathbf{D}\overline{\mathbf{v}}_{n+1} = 0 \tag{16}$$

where $\overline{\mathbf{r}}_m$ and $\overline{\mathbf{r}}_c$ are the residuals of the momentum and continuity equations, respectively, $\mathbf{M}$ is the mass matrix, $\mathbf{L}$ is the Laplacian matrix, $\mathbf{G}$ is the gradient matrix, $\mathbf{D}$ is the divergence matrix, $\overline{\mathbf{K}}(\overline{\mathbf{v}}_{n+1})$ is the non-linear convection operator, $\overline{\mathbf{v}}$ and $\overline{p}$ are the velocity and pressure respectively and $\overline{\mathbf{F}}$ is the external force vector. The matrices are assembled from the elemental contributions defined as

$$M_i^{ab} = \rho_f \int_{\Omega_e} N^a N^b d\Omega \tag{17}$$

$$L^{ab} = \int_{\Omega_e} \frac{\partial N^a}{\partial x_i}\frac{\partial N^b}{\partial x_i} d\Omega \tag{18}$$

$$G_i^{ab} = -\int_{\Omega_e} \frac{\partial N^a}{\partial x_i} N^b d\Omega \tag{19}$$

$$K^{ab} = \rho_f \int_{\Omega_e} N^a \left(\overline{\mathrm{v}}_i \frac{\partial N^b}{\partial x_i}\right) d\Omega \tag{20}$$

$$F_i^a = \rho_f \int_{\Omega_e} N^a g_i d\Omega - \int_{\Gamma_l} p_A N^a n_i d\Gamma - \int_{\Gamma_l} \gamma\kappa N^a n_i d\Omega \tag{21}$$

$$D_i^{ab} = \int_{\Omega_e} N^a \frac{\partial N^b}{\partial x_i} d\Omega \tag{22}$$

where N^a stands for the standard linear FE shape function at node a and Ω_e is the element integration domain. Indexes i,j refer to spatial components. The Laplacian matrix $\mathbf{L}$ has been integrated by parts, thus allowing us to use low-order interpolation functions for velocity and pressure. In the present work, both velocity and pressure have been approximated by linear Lagrangian functions (i.e., P1P1 elements have been chosen). This leads to lower system sizes and therefore to solutions with lower computational cost. However, since the order of interpolation is the same for both variables, pressure stabilization is implemented [23]. Detailed information on stabilization techniques can be found in Refs. [24] and [25].

The discretized governing equations (Eqs. (15) and (16)) are valid for either sub-domain (Ω_A and Ω_W). Note that in Ref. Ω_W due to using a Lagrangian framework for the water domain, (a) the convective term $\overline{\mathbf{K}}$ is equal to zero and (b) the elemental integration domains in Eqs. (17)–(22) must be updated according to current mesh configuration.

Note that the set of discretized governing equations has been written in residual form. This form is adopted to solve Eqs. (15) and (16) using a Newton-Raphson method. In the present work the governing equations are solved in two dimensions.

2.3.2. Time step restrictions

The explicit treatment of the surface tension term leads to severe restrictions upon the critical time step size in the simulation of dynamic problems [12,22]. It is governed by the capillary time step [11,12,26]:

$$\Delta t < \sqrt{\frac{\rho_A + \rho_W}{(2\pi)^3 \gamma} h^3} \tag{23}$$

where ρ_A and ρ_W are the densities of the gas and liquid phase, respectively, γ is the surface tension coefficient between phases, and h is the element size. For PEFC channels (1×1 mm cross-section), a typical droplet is ~10^{-4} m in height. Considering a mesh based on elements of 10^{-6} m, the critical time step would be of the order of 10^{-8} s.

To eliminate this restriction, the surface tension term is treated implicitly in this work. The last term in Eq. (21) is linearized with respect to the kinematic variable and then is added to the left-hand side (tangent) matrix according to [22]. In the residual, the surface tension term is recomputed at every non-linear iteration according to the updated mesh position of the Lagrangian domain.

2.3.3. Summary

The overall solution of the coupled air-water problem can be summarized as follows. Let us consider that the solution (velocity $\overline{\mathbf{v}}_n$ and pressure $\overline{p}_n$) is known at the time step t_n in both air and water domains. To find the velocity and pressure at t_{n+1} the following algorithm is implemented:

1. Solve water droplet problem (Eqs. (15) and (16) in Ω_W). A new domain position and variables solution, $\overline{\mathbf{v}}_{n+1}$ and $\overline{p}_{n+1}$, for water is obtained.
2. Identify the position of the Lagrangian domain within the Eulerian one using an oct-tree approach [17].
3. Impose the water velocity at the interface onto the air domain (weak Dirichlet boundary condition, see Ref. [17])
4. Solve the air problem in Ω_A, obtaining velocity, $\overline{\mathbf{v}}_{n+1}$, and pressure, $\overline{p}_{n+1}$, of air.
5. Project the air pressure and the viscous stress onto boundary of droplet and compute the corresponding force term (Neumann boundary condition).
6. Go to next time step

2.4. Implementation

The method was implemented within *Kratos Multi-Physics*, a C++ object oriented FE framework [27]. Newton-Rapshon method is used to solve Eqs. (15) and (16). The resulting system of equations is solved using the Bi-conjugate gradient stabilized method (BICGSTAB). This method is known for its improved rate of convergence and low computational cost when compared to other iterative methods (such as Conjugate Gradient Squared (CGS), Biconjugate Gradient (Bi-CG) or Generalized Minimum Residual (GMRES)) [28].

2.5. Input parameters

Table 1 shows the input parameters used in the model, such as absolute and relative tolerances for pressure and velocity solvers and maximum number of iterations. Table 2 includes water and air properties used in the simulations. In addition to the fluid properties, droplet volume and static contact angle are also used as input parameters. The static contact angle is a function of the type of substrate used and must be determined experimentally by sessile micro-droplet experiments.

3. Results and discussion

Results were obtained using a Linux 12.04 box with an Intel® Core™ i5 CPU M450 @ 2.40Ghz with 4 processors. Computational time is different on each example. Sessile drop examples only involved the solution of the Lagrangian domain, and the cost was remarkably low. Depending on the droplet size, simulations in these examples took between 20 and 120 s. Droplet oscillation in a PEFC channel simulations took between 90 and 180 min to simulate a real time period of 1 s in one CPU, i.e., the code is not parallel.

In the following examples the volume of the droplet is included as input data. Since the present work considers a 2D model, the volume corresponds to the volume of a spherical cap of radius R and static contact angle θ_S. Using trigonometry, it can be shown that the volume of the spherical cap is equal to:

$$V = R^3 \left[\frac{4}{3}\pi - \frac{\pi}{3}(1 + \cos\theta_S)^2 (2 - \cos\theta_S) \right] \tag{24}$$

3.1. Sessile drop

The first example aims to validate experimentally the numerical

Table 1
Input parameters used in the velocity and pressure solvers.

Parameter	Value
Velocity iterative tolerance	10^{-6}
Pressure iterative tolerance	10^{-3}
Velocity solver max number of iterations	5000
Pressure solver max number of iterations	1000
Velocity relative tolerance	10^{-3}
Velocity absolute tolerance	10^{-5}
Pressure relative tolerance	10^{-2}
Pressure absolute tolerance	10^{-4}
Linear solver iterative tolerance	10^{-4}
Linear solver max number of iterations	5000

model by characterizing a sessile drop. The contact angle for the sessile drop is measured using a commercial drop shape analyzer (Kruss DSA 100E, Kruss GmbH, Hamburg, Germany). Details of the injection process can be found in Ref. [29]. A water droplet of a given volume was injected on top of a gas diffusion layer (SIGRALET 24BC, GDL side). The experiment was performed with droplets of volumes ranging from 3 to 30 μl. In order to find the static contact angle of the droplet with the surface, the smallest droplet (3 μl volume) was generated at the tip of the needle. The droplet of given volume was brought near to the membrane and allowed to spread. After attaining the equilibrium contact angle, the needle was retracted and the contact angle measurements were preformed.

After the injection process was finished, a snapshot of the resulting droplet was taken at different time instances (Fig. 3(a)–(c)). Using ImageJ software [30] together with DropShape [31], the static contact angle was estimated (Fig. 3(d)). The measured angle of $\theta_s = 135$ deg was used as a reference for the rest of the examples for the contact angle condition.

For the simulation of each sessile droplet, a spherical cap with radius R and contact angle $\theta_S = 135$ deg was used as the initial droplet shape used to generate the Lagrangian mesh that represents the droplet. For a given droplet volume, the radius R was found using Eq. (24). After a simulation of 1s, the steady-state configuration of the droplet was taken as the deformed shape to compare with the experiments.

Fig. 4(a) shows a direct comparison of numerical and experimental results. In order to provide a more detailed comparison, the x and y scales have been normalized to compare other droplet volumes. In Fig. 4(b) and (c) the x scale goes from 0 to -1, being 0 the center of the droplet and -1 the minimum x coordinate. The coordinates are taken from a spherical cap, meaning that a curve that passes through the points $x_{\text{norm}} = -1$ and $y_{\text{norm}} = 1$ is a perfect spherical cap. Fig. 4(b) shows that the 3 μl drop obtained experimentally is a perfect spherical cap, which means that for this droplet size surface tension dominates over gravity. The numerical simulation using the method proposed here predicts a slightly more deformed droplet.

Other droplet volumes ranging from 5 to 30 μl have been compared with experimental data. As the droplet volume increases, gravity effects become more evident. Fig. 4(c) shows the comparison between numerical and experimental results obtained with a 30 μl-volume droplet. Overall, the obtained numerical profiles show good agreement with experimental data.

Table 3 shows the relative errors of contact angle (ε_θ), drop height (ε_h) and chord (ε_c) of numerical results compared to experimental data. Two numerical models have been used. The former is based on a fixed value of the equilibrium contact angle ("fix" columns), which corresponds to the aforementioned value of 135 deg. In the latter, a variable value of the contact angle is taken. The contact line undergoes pinning as long as the contact angle is lower than 162 deg. In other words, this threshold value is considered as the advancing contact angle.

Results in Table 3 show that if the phenomenon is modeled considering a dynamic contact angle, the error is considerably reduced. This is not the case for the 3 μl example, however, because in this case gravity effects are negligible and therefore the contact angle remains constant. In this article, the droplet is directly placed on the substrate. Santamaria et al. [32] recently showed that the contact angle might change if water emerges directly from a GDL pore. Droplet emergence from a pore can also be studied using the proposed formulation and it will be the focus of a future publication. Some preliminary qualitative results for the droplet injection have been obtain in Ref. [33].

Table 2
Fluid's properties used in the simulations, taken at a reference temperature and pressure of $T = 298$ K and $p = 1$ atm, respectively.

Variable	Symbol	Value	Units
Water density	ρ_w	1000	kg m^{-3}
Water viscosity	μ_w	10^{-3}	kg m^{-1} s^{-1}
Air density	ρ_{air}	1.205	kg m^{-3}
Air viscosity	μ_{air}	1.98×10^{-5}	kg m^{-1} s^{-1}
Surface tension	γ	0.072	N m^{-1}
Gravity	**g**	9.81	m s^{-2}

3.2. Sessile drop on an inclined plane

This example aims to show the effects of contact angle hysteresis and pinning observed when an external force (such as gravity or air flowing) acts on a droplet. The sessile drop example is repeated but introducing a slight difference: the droplet is laying on an inclined plane. A Kruss DSA 100E droplet analyzer equipped with an external tilt table (Kruss GmbH, Hamburg, Germany) is used to perform the measurements. A drop is placed on a GDL (SIGRALET 24BC, GDL side) using the process described in the previous section, and then the drop stage is tilted at a constant rate of 0.4 deg s^{-1}.

Fig. 5 displays the simulation results obtained for a 30 μl-volume droplet during the deformation process. Initially, the droplet profile is symmetric, i.e., the hysteresis angle, θ, is zero, and is deformed in the vertical direction due to gravity effects. As the tilting process starts, the receding contact angle (left) diminishes, whereas the advancing contact angle (right) increases, leading to an increase in the hysteresis angle.

Fig. 6(a)–(c) show the comparison between the measured contact angles (red square and blue diamond markers) and the modeled values (red solid and blue dashed lines). In these plots, *REC* and *ADV* stand for receding and advancing contact angles, respectively. Results show that numerical values agree well with experimental data. For each droplet volume, detachment can be read directly from its corresponding plot, and it occurs when the tilt angle reaches its maximum value. For instance, the 10 μl droplet detaches when the plane is tilted 36 deg, and the advancing and receding angles are 149 and 115 deg, respectively.

3.3. Droplet oscillation in a PEFC channel

Droplet oscillation has been studied since the mid-1800s. Early works of Lord Rayleigh and Lamb [35] on free drop oscillation revealed that surface tension and inertial forces produced a balancing-unbalancing process, yielding drop oscillations. Recent studies on droplet dynamics in PEFC show that oscillations are responsible for droplet detachment [6,7,19,34].

A review on droplet oscillation can be found in Chapter 5 of Milne's work [34]. This review is focused on constrained droplet oscillation (i.e., droplets sitting on surfaces, as shown in the first example). When a constrained droplet oscillates, surface oscillation is coupled to oscillation of the center of mass [34]. Thus, in this article, droplet oscillations will be measured by the displacements of the center of mass in x and y directions.

3.3.1. Validation

Milne's work [34] showed an experimental setup of a Teflon surface in a wind tunnel where a water droplet was placed. In the experiment, droplet oscillations were induced by gas-flow. For different droplet volumes, the frequency of oscillation was observed. Several air velocity values were used in the experiments, and the obtained values did not depend on the air velocity. No data was provided to support this observation. The current model has

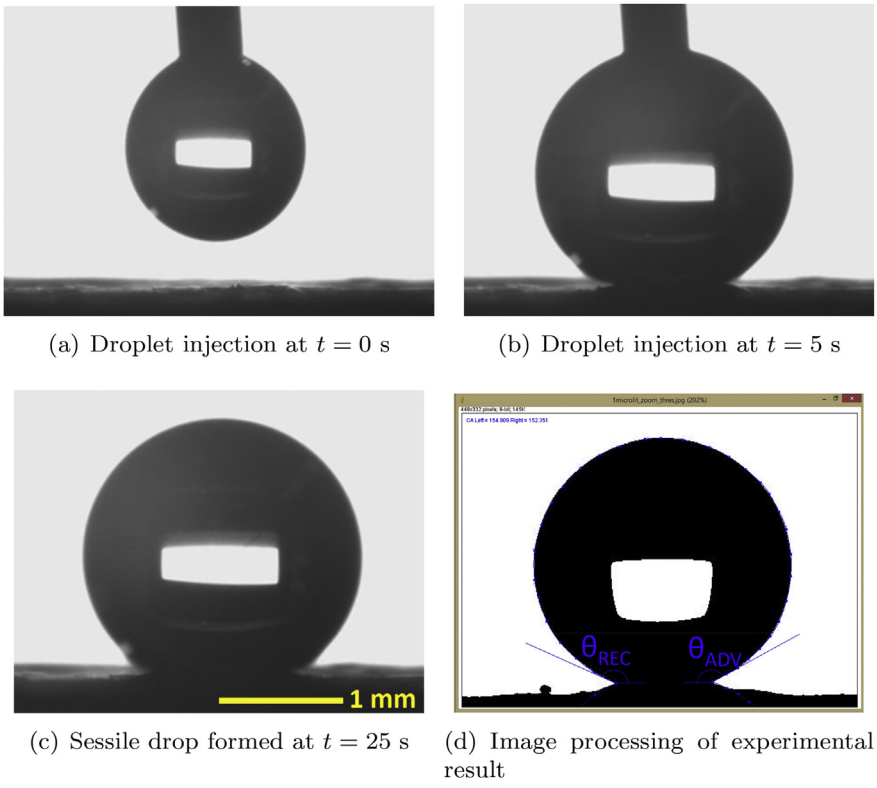

(a) Droplet injection at $t = 0$ s (b) Droplet injection at $t = 5$ s

(c) Sessile drop formed at $t = 25$ s (d) Image processing of experimental result

Fig. 3. Injection process of a droplet on a hydrophobic surface. All images have the same scale.

been used to validate this result. For a droplet of 13 μl volume, simulations were performed at varying air velocities and the droplet vibrational frequency was obtained. Droplet frequency of oscillation remained relatively constant for all simulations. In every case, oscillation is measured as the x and y displacement of the node corresponding to the droplet's centroid.

The current example reproduces the experiment from Milne's study. The channel is modeled as a rectangle where air flows in the positive x-direction. Air enters the channel at $v_{air} = 6$ m s^{-1} and the right side of the channel is considered an open boundary (no viscous stress on the normal direction). Channel is 50 mm length and its height depends on the droplet size considered. In order to make sure that wall effects do not affect results, droplet height is lower than 10% of channel's height [7]. On the other hand, a small droplet of volume ranging from 13 to 100 μl is located at the center of the channel. Droplet pinning is forced by imposing zero-velocity at the lower boundary of the droplet. The numerical setup used in the simulations is similar to that from Fig. 1 in Ref. [7]. A 1 s simulation is performed with $\delta t = 10^{-3}$ s. The evolution of shape, pressure profile and velocity distribution for the 13 and 100 μl-volume droplets are depicted in Fig. 7.

Similar behavior is observed for the considered droplet volumes. One can observe a hydrostatic pressure profile within the droplet, with mild oscillations due to the air flowing around the droplet. After a certain time, the droplet reaches some sort of steady state. At that moment, the drag exerted by the air is deforming the droplet, whereas the adhesion force is opposing this force and trying to take the droplet to a new equilibrium state. A recirculation pattern can be observed in Fig. 7(d) and (i). This phenomenon has been observed experimentally in Ref. [36]. Recirculation appears as a consequence of the viscous forces acting on the air-water interface. A no-slip boundary condition is applied for air velocity at the channel walls (Eq. (4)), however, at the air/liquid interface, a zero velocity jump is imposed (Eq. (6)). Since the airflow velocity is not zero at the vicinity of the droplet, it induces water movement in the same direction initiating the observed recirculation pattern.

Fig. 6(d) shows the frequency of oscillation in x and y directions observed at the droplet's center of mass for several droplet volumes. Numerical results (square and triangle markers) are compared to experimental data (represented by solid and dashed lines) from Ref. [34] and they show good agreement. It is important to note that the relationship between frequency of oscillation and droplet volume is exponential. Transforming x axis in Fig. 6(d) into the inverse of the square root of volume, this relationship becomes linear.

Larger droplets have lower values of oscillation frequency, as already reported in Refs. [6] and [34]. Results also show that in the limit case, a zero value of frequency is achieved by an infinitely large drop [34]. Fig. 6(d) also shows numerical results obtained with the semi-analytical model developed by the authors in Ref. [7] (cross markers). The semi-analytical model estimates frequencies that are in reasonable agreement with computational and experimental observations thereby further validating the model compared to the results of Esposito et al. [6] which reported much higher frequencies. Even though the predictions are in relatively good agreement, the semi-analytical model is not able to provide the degree of accuracy provided by the numerical model, especially as the volume of the droplet increases. The semi-analytical model assumed a predefined shape and did not consider gravitational effects. The former might be responsible for the discrepancies for small droplet volumes while the latter may be the cause of the differences for larger droplets.

3.3.2. Droplet detachment

In this article, the critical velocity for four different droplet geometries is studied by varying the airflow rate until droplet

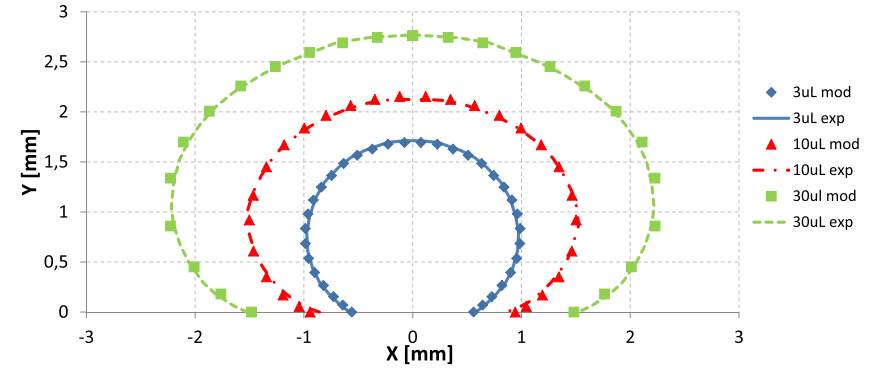

(a) 3, 10 and 30 μl-volume droplets

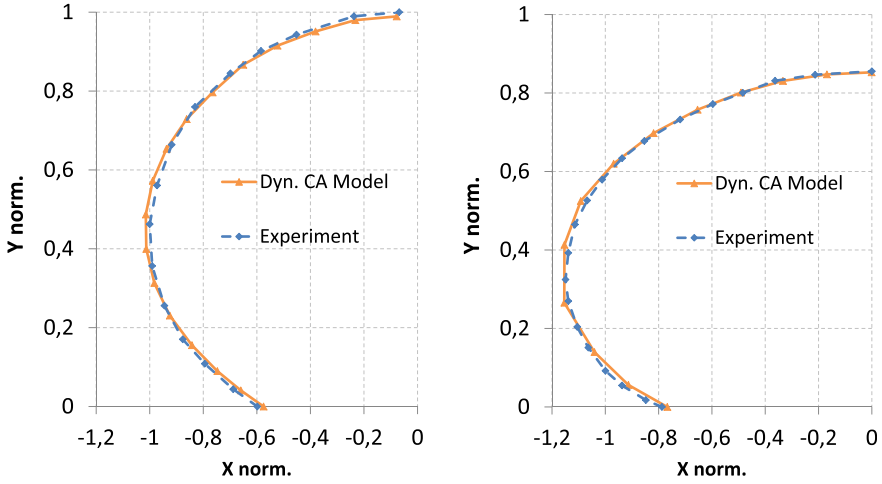

(b) 3 μl droplet (c) 30 μl droplet

Fig. 4. Comparison between modeled and experimental droplets with volumes from 3 to 30 μl using a scale in mm (top) and normalized (bottom), using pinning with variable contact angle.

detachment occurred. Based on this value, a critical velocity was obtained. The area coverage is obtained also from the simulation by computing the area of the drop in contact with the GDL. The detachment time is obtained by taking into account the volume of the droplet and that at 1 A cm^{-2}, the drop would fill at a mass flow rate of $\dot{Q} = 0.047$ μl s^{-1}. The channel is modeled as a 1 $\times$ 10 mm rectangle.

A comparison between two models (numerical and semi-analytical, see Ref. [7]) developed by the authors is included in Table 4. Detachment times are in agreement between the two models, as well as critical velocities for detachment. The semi-analytical model predicts higher values of critical air velocity for small droplets. On the other hand, for droplets close to channel blockage the critical air velocity is underpredicted. The semi-analytical droplet model does not include pressure effects, and pressure deforms the droplet in the vertical direction, as shown in Fig. 8(d). The numerical model predicts a more deformed droplet and therefore critical velocity for detachment is higher when compared to semi-analytical results. Unfortunately, no time detachment studies were found in literature using VOF method and our results cannot be compared to previous works.

For the considered droplet sizes and flow conditions, the Reynolds numbers obtained at the onset of detachment range between 300 and 1000. Reynolds numbers have been computed considering the channel height as the characteristic length.

Table 4 shows that the detachment velocity increases with decreasing droplet size. Therefore, for high air flow rate conditions, e.g., operation at high stoichiometry or at high current density, liquid water will be rejected as small droplets. At low flow rates, however, droplet detachment will not occur until the droplet has reached a much larger size. For example, assuming a fuel cell operating with humid air (T = 80◦C and RH = 90%) at a stoichiometry of 3, the droplet height will reach 70% of the channel height at a current density of 1.38 Acm^{-2} (detachment velocity of 5.12 m s^{-1}).

Fig. 8 depicts droplet profiles (blue solid and black dashed lines) and air velocity distribution (red dashed line) prior to detachment.

Table 3
Relative error between numerical and experimental results with respect to contact angle (ε_θ), height (ε_h) and chord (ε_c) for different droplet volumes (V), considering fixed (fix) and dynamic (dyn) contact angles.

V [μl]	ε_θ [%]		ε_h [%]		ε_c [%]	
	fix	dyn	fix	dyn	fix	dyn
3	−1.40	−1.40	−2.42	−2.42	13.14	13.14
5	−7.56	−3.22	0.07	−0.27	25.00	2.84
10	−6.35	−2.49	−5.64	−4.18	23.93	7.73
20	−8.48	−3.45	−1.13	−6.28	27.67	7.89
30	−4.77	−2.50	−3.43	−2.60	9.66	3.11

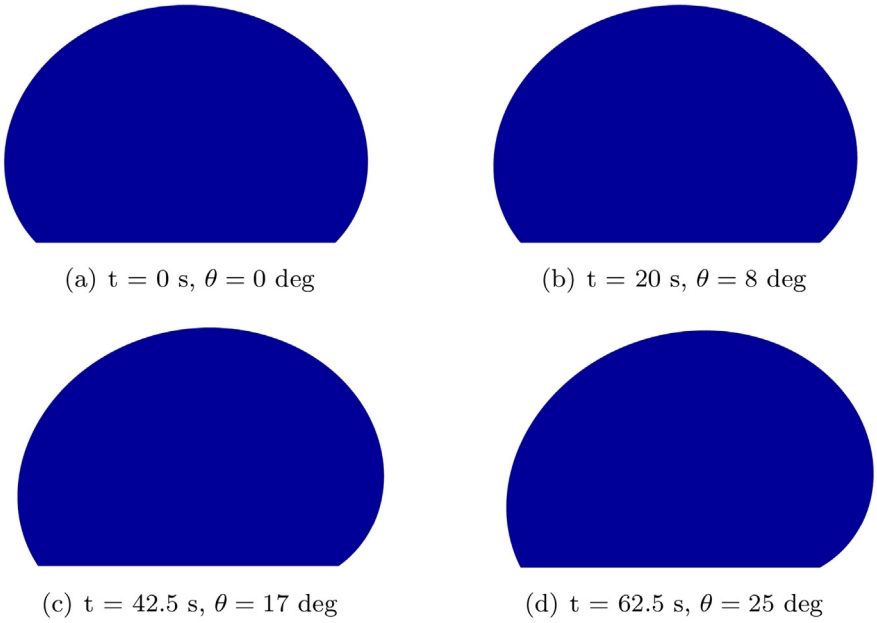

(a) t = 0 s, $\theta = 0$ deg (b) t = 20 s, $\theta = 8$ deg

(c) t = 42.5 s, $\theta = 17$ deg (d) t = 62.5 s, $\theta = 25$ deg

Fig. 5. Resulting animation of the modeled droplet during deformation process.

Primary horizontal axis (bottom) represents x coordinate, whereas air velocity is represented by secondary horizontal axis (top). Two different substrates have been considered in order to see the effects of substrate properties on droplet deformation prior to detachment. The first surface is a flat Teflon surface. Due to the smooth hydrophobic surface, all modeled droplets detach without undergoing severe deformation (black dashed lines in Fig. 8 labeled as "Teflon"). The second substrate corresponds to the GDL considered in Sections 3.1 and 3.2. Since the GDL is a rough surface, the adhesion force of the droplet increases. This is manifested by its deformation in both x and y directions (blue solid lines in Fig. 8 labeled as "GDL"). Although all the considered droplet's heights are below 1 mm (and therefore surface tension effects are dominant) pressure effects appear, deforming the droplets in y direction. These effects have also been reported in literature (e.g. see Ref. [32]).

4. Conclusions

A numerical study of droplet dynamics using an embedded

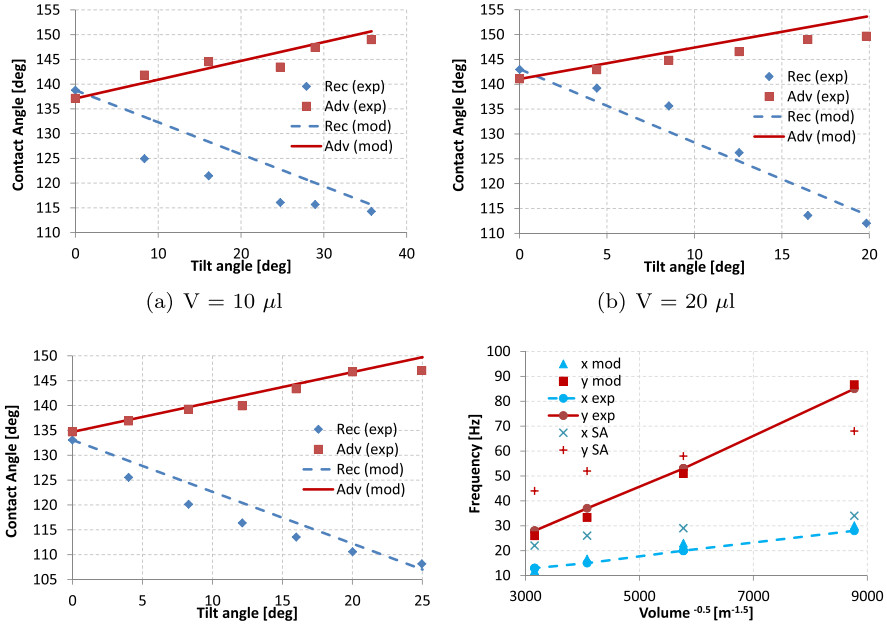

(a) V = 10 μl (b) V = 20 μl

(c) V = 30 μl (d) Frequency vs. Volume$^{-0.5}$

Fig. 6. (a)–(c) Comparison between the measured contact angle (square and diamond markers) and the modeled contact angle (solid and dashed lines), (d) Oscillation frequency versus the inverse of the square root of droplet volume, according to experiments (exp), numerical model (mod) and semi-analytical model (SA). Droplet volumes of 13, 30, 58 and 100 μl have been used to reproduce the results from Ref. [34].

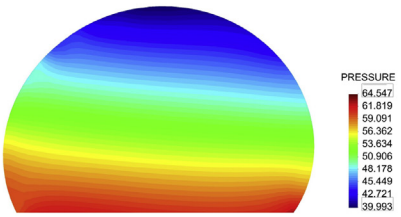

(a) Pressure profile at $t = 0$ s

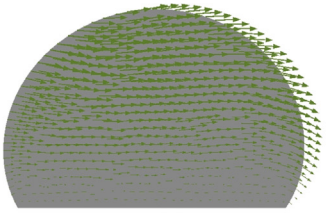

(b) Velocity field at $t = 0$ s

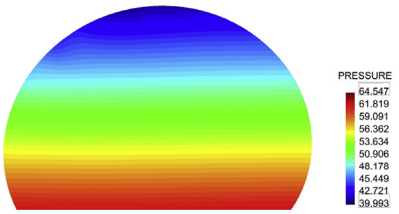

(c) Pressure profile at $t = 0.25$ s

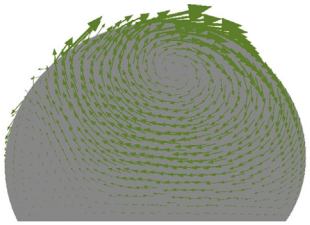

(d) Velocity field at $t = 0.25$ s

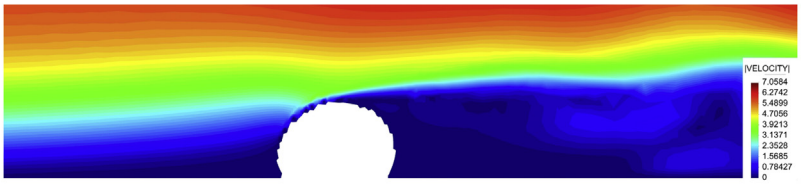

(e) Airflow velocity field at $t = 0.25$ s

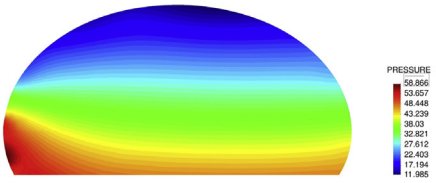

(f) Pressure profile at $t = 0$ s

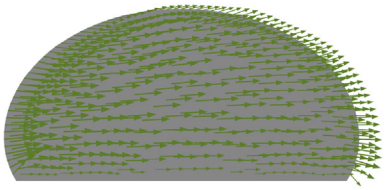

(g) Velocity field at $t = 0$ s

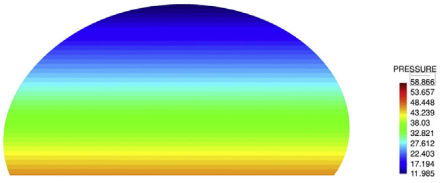

(h) Pressure profile at $t = 0.25$ s

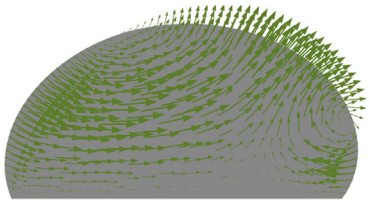

(i) Velocity field at $t = 0.25$ s

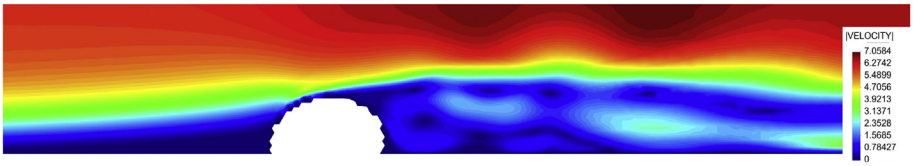

(j) Airflow velocity field at $t = 0.25$ s

Fig. 7. (a)–(d) and (f)–(i) Evolution of pressure and velocity fields in the 13 and 100 μl-volume droplets, respectively; (e) and (j) airflow velocity field at the vicinity of the considered droplets within a PEFC channel.

Table 4
Critical air velocity (v_{det}), detachment time (t_{det}) and area covered (A_{cov}) for different droplet heights (h) according to current model and semi-analytical model presented in Ref. [7].

h [mm]	Numerical model			Semi-analytical model		
	v_{det} [m s^{-1}]	t_{det} [s]	A_{cov} [mm^2]	v_{det} [m s^{-1}]	t_{det} [s]	A_{cov} [mm^2]
0.17	14.98	0.07	0.014	15.85	0.08	0.016
0.31	11.06	0.52	0.053	11.27	0.55	0.055
0.52	8.28	1.62	0.113	6.79	2.37	0.146
0.70	5.12	4.73	0.231	4.52	5.79	0.264

Lagranian-Eulerian formulation has been developed and validated experimentally. Results show that the embedded formulation is very advantageous computationally, allowing the solution of droplet deformation problems in an air stream using time steps several orders of magnitude higher than those used in existing Eulerian formulations using the volume of fluid (VOF) method previously described in the literature.

The analysis of a sessile droplet laying on a rough surface shows that the numerical error is reduced when a dynamic contact angle condition is used. For rough surfaces, such as the ones encountered in PEFC channels, a static contact angle condition leads to significant numerical errors. Whereas the droplet chord length error can be as high as 25% when a static contact condition is used, the proposed dynamic contact angle condition reduces the error to 3%. Results from a droplet in a tilted plane also show that numerical predictions of advancing and receding angles are in reasonable agreement with experimental results.

A sessile droplet subjected to an airflow is also studied. Numerically predicted oscillations are consistent with previous works [6,7,34]. A simulation of 1 s has been performed considering several droplet volumes, and the obtained numerical results agree well with experimental observations from Ref. [34]. This result is particularly important since droplet oscillation is responsible for droplet detachment [6,7,34,19]. A recirculation pattern is also observed within the droplet when it reaches steady-state, as observed by Minor's experiments [36].

The new model is compared to our previously proposed semi-analytical model [7]. Results show the same trend with larger droplets having lower frequencies of oscillation. However, differences between semi-analytical model and experimental results are evident for high droplet volumes. These differences are probably caused by the absence of gravity effects and the assumed geometry used in the semi-analytical model. For small droplets similar to those observed in fuel cell channels where gravity effects are negligible, the semi-analytical model shows good predictive capabilities.

A study on the sensitivity of droplet detachment to airflow velocity shows that larger droplets exhibit lower values of critical air velocity for detachment, but the time that takes to reach this condition is longer. Time detachment results are also obtained with the semi-analytical model and are in good agreement with those found using the current numerical model. A slight difference between critical air velocity predicted values is observed in extreme cases (lower and higher droplet heights) but the same trends are observed with both models. The effect of substrate wettability and roughness on droplet deformation prior to detachment was also studied. Whereas droplets on top of rough surfaces, such as GDLs, undergo large deformations in both x and y directions prior to

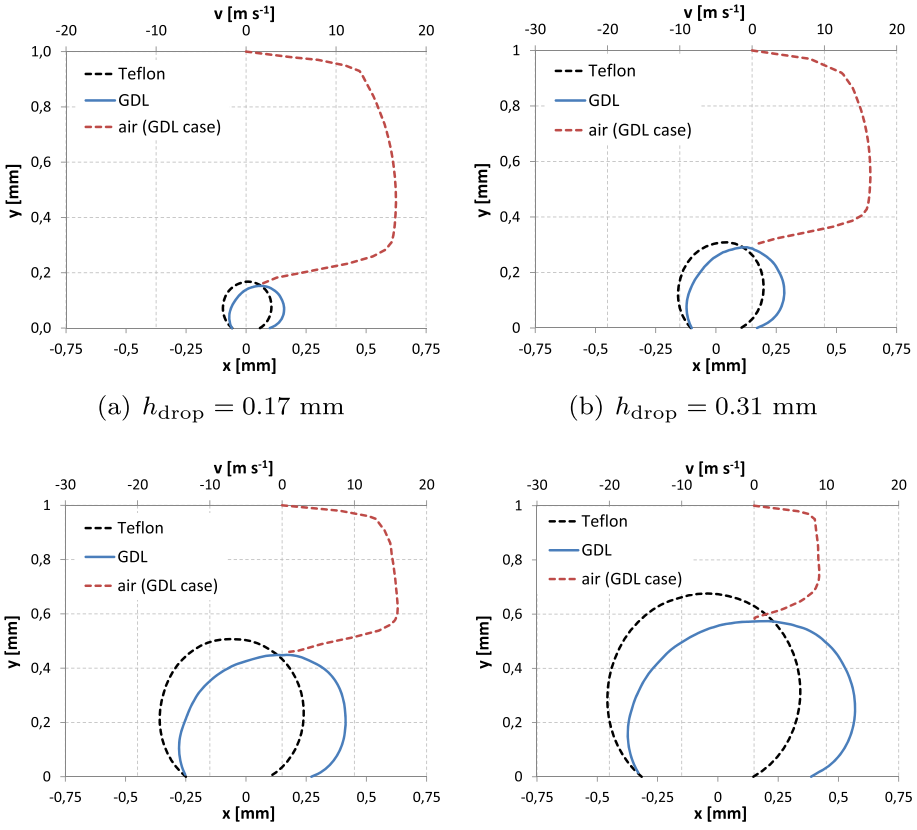

(a) $h_{\mathrm{drop}} = 0.17$ mm (b) $h_{\mathrm{drop}} = 0.31$ mm

(c) $h_{\mathrm{drop}} = 0.52$ mm (d) $h_{\mathrm{drop}} = 0.70$ mm

Fig. 8. Drop (solid line) and air velocity (dashed line) profiles at detachment in a PEFC channel.

detachment, droplets on smooth hydrophobic surfaces detach sooner and almost without deforming.

The effects of water injection rate were not studied, and they are left for future work. This work is performed in 2D, this assumes that the out-of-plane forces are equal and in opposite directions thereby not affecting the droplet force balance and the highest cross-sectional area dominates the force balance. For droplets near channel walls these assumptions break down and 3D simulations are required. This will be the subject of our future research. The present model is also limited to the onset of droplet detachment, therefore, in its current form, it cannot predict the post-detachment behavior and the corresponding interactions with the wall. The embedded setting however can, in theory, handle droplet motion and large deformation by implementing appropriate boundary conditions in the Lagrangian mesh.

Acknowledgments

This work has been supported by the FPI Research Grant BES-2011-047702 subject to the Spanish Project BIA2010-15880, by COMETAD project of the National RTD Plan (ref. MAT2014-60435-C2-1-R), from the *Ministerio de Economía y Competitividad* (*grant no: FDPI-2013-18471*) and the Natural Science and Engineering Research Council of Canada (NSERC) (grant no: 371088-10) Discovery grant.

References

[1] X. Zhu, P.C. Sui, N. Djilali, Dynamic behaviour of liquid water emerging from a GDL pore into a PEMFC gas flow channel, J. Power Sources 172 (2007) 287–295.
[2] J. Carton, V. Lawlor, A. Olabi, C. Hochenauer, G. Zauner, Water droplet accumulation and motion in PEM (Proton Exchange Membrane) fuel cell mini-channels, Energy 39 (2012) 63–73.
[3] A.Z. Weber, R.L. Borup, R.M. Darling, P.K. Das, T.J. Dursch, W. Gu, D. Harvey, A. Kusoglu, S. Litster, M.M. Mench, R. Mukundan, J.P. Owejan, J.G. Pharoah, M. Secanell, I.V. Zenyuk, A critical review of modeling transport phenomena in Polymer-Electrolyte fuel cells, J. Electrochem. Soc. 161 (12) (2014) F1254–F1299.
[4] K. Chen, M. Hickner, D. Noble, Simplified models for predicting the onset of liquid water droplet instability at the gas diffusion layer/gas flow channel interface, Int. J. Energy Res. 29 (12) (2005) 1113–1132.
[5] E. Kumbur, K. Sharp, M. Mench, Liquid droplet behavior and instability in a polymer electrolyte fuel cell flow channel, J. Power Sources 161 (2006) 333–345.
[6] A. Esposito, P. Polverino, C. Pianese, Y. Guezennec, A lumped model of single droplet deformation, oscillation and detachment on the GDL surface of a PEM fuel cell, ASME 2010 8th International Fuel Cell Science, Engineering and Technology Conference.
[7] A. Jarauta, M. Secanell, J. Pons-Prats, P.B. Ryzhakov, S.R. Idelsohn, E. Oñate, A semi-analytical model for droplet dynamics on the GDL surface of a PEFC electrode, Int. J. Hydrogen Energy 40 (2015) 5375–5383.
[8] A. Theodorakakos, T. Ous, M. Gavaises, J. Nouri, N. Nikolopoulos, H. Yanagihara, Dynamics of water droplets detached from porous surfaces of relevance to PEM fuel cells, J. Colloid Interface Sci. 300 (2006) 673–687.
[9] C. Hirt, B. Nichols, Volume of Fluid (VOF) method for the dynamics of free boundaries, J. Comput. Phys. 39 (1981) 201–225.
[10] R.B. Ferreira, D.S. Falcão, V.B. Oliveira, A.M.F.R. Pinto, Numerical simulations of two-phase flow in proton exchange membrane fuel cells using the volume of fluid method - a review, J. Power Sources 277 (2015) 329–342.
[11] J. Brackbill, D. Kothe, C. Zemach, A continuum method for modeling surface tension, J. Comput. Phys. 100 (1992) 335–354.
[12] M. Sussman, M. Ohta, A stable and efficient method for treating surface tension in incompressible two-phase flow, SIAM J. Sci. Comput. 31 (2009) 2447–2471.
[13] P.H. Saksono, D. Perić, On finite element modelling of surface tension. Variational formulations and applications - Part I: quasistatic problems, Comput. Mech. 38 (2006) 265–281.
[14] P.H. Saksono, D. Perić, On finite element modelling of surface tension. Variational formulations and applications - Part II: dynamic problems, Comput. Mech. 38 (2006) 251–263.
[15] M. Mier-Torrecilla, Numerical Simulation of Multi-fluid Flows with the Particle Finite Element Method, Ph.D. thesis, Universitat Politècnica de Catalunya, 2010.
[16] J. Marti, P. Ryzhakov, S. Idelsohn, E. Oñate, Combined Eulerian-PFEM approach for analysis of polymers in fire situations, Int. J. Numer. Methods Eng. 92 (2012) 782–801.
[17] P. B. Ryzhakov, A. Jarauta, An embedded approach for immiscible multi-fluid problems, Int. J. Numer. Methods Fluidsdoi:10.1002/fld.4190.
[18] X. Zhu, P. Sui, N. Djilali, Numerical simulation of emergence of a water droplet from a pore into a microchannel gas stream, Microfluid Nanofluid 4 (2008) 543–555.
[19] X. Zhu, P. Sui, N. Djilali, Three-dimensional numerical simulations of water droplet dynamics in a PEMFC gas channel, J. Power Sources 181 (2008) 101–115.
[20] J. Israelachvili, Intermolecular and Surface Forces, third ed., Elsevier, 2011.
[21] M. Bellet, Implementation of surface tension with wall adhesion effects in a three-dimensional finite element model for fluid flow, Commun. Numer. Methods Eng. 17 (2001) 563–579.
[22] P.J. Slikkerveer, E.P.V. Lohuizen, S.B.G. O'Brien, An implicit surface tension algorithm for Picard solvers of surface-tension-dominated free and moving boundary problems, Int. J. Numer. Methods Fluids 22 (1996) 851–865.
[23] R. Codina, Stabilization of incompressibility and convection through orthogonal sub-scales in finite element methods, Comput. Methods Appl. Mech. Eng. 190 (2000) 1579–1599.
[24] J. Donea, A. Huerta, Finite Element Methods for Flow Problems, first ed., John Wiley & Sons, 2003.
[25] R. Codina, A stabilized finite element method for generalized stationary incompressible flows, Comput. Methods Appl. Mech. Eng. 190 (20–21) (2001) 2681–2706, http://dx.doi.org/10.1016/S0045-7825(00)00260-7. URL, http://www.sciencedirect.com/science/article/pii/S0045782500002607.
[26] S. Hysing, A new implicit surface tension implementation for interfacial flows, Int. J. Numer. Methods Fluids 6 (51) (2006) 659–672.
[27] P. Dadvand, R. Rossi, E. Oñate, An object-oriented environment for developing finite element codes for multi-disciplinary applications, Arch. Comput. Methods Eng. 17 (3) (2010) 253–297.
[28] C. Kelley, Iterative Methods for Linear and Nonlinear Equations, first ed., SIAM, 1995.
[29] P.R. Waghmare, S.K. Mitra, Contact angle hysteresis of microbead suspensions, Langmuir 26 (22) (2010) 17082–17089.
[30] ImageJ, Image Processing and Analysis in Java, http://imagej.nih.gov/ij/, accessed: 2015-03-16.
[31] A. Stalder, G. Kulik, D. Sage, L. Barbieri, P. Hoffmann, A snake-based approach to accurate determination of both contact points and contact angles, Coll. Surfaces A Physicochem. Eng. Aspects 286 (1–3) (2006) 92–103.
[32] A.D. Santamaria, P.K. Das, J.C. MacDonald, A.Z. Weber, Liquid-water interactions with gas-diffusion-layer surfaces, J. Electrochem. Soc. 161 (12) (2014) F1184–F1193.
[33] P. Ryzhakov, A. Jarauta, M. Secanell, J. Pons-Prats, On the application of the PFEM to droplet dynamics modeling in fuel cells, Comput. Part. Mech. doi:10.1007/s40571-016-0112-9.
[34] A. Milne, A. Amirfazli, Drop shedding by shear flow or hydrophilic to superhydrophobic surfaces, Langmuir 25 (24) (2009) 14155–14164.
[35] H. Lamb, Hydrodynamics, fourth ed., Cambridge University Press, Cambridge, 1916. URL, https://books.google.es/books?id=d_AoAAAAYAAJ.
[36] G. Minor, Experimental Study of Water Droplet Flows in a Model PEM Fuel Cell Gas Microchannel, Ph.D. thesis, University of Victoria, 2007.